Supporting information

Towards Large-Scale Electrochemical Energy Storage in the Marine with Highly-Extensible "Paper-Like" Seawater Supercapacitor Device

Situo Cheng[1#], Zhe Dai[1#], Jiecai Fu[1]*, Peng Cui[1], Kun Wei[1], Yaxiong Zhang[1], Yin Wu[1], Yupeng Liu[1], Zhenheng Sun[1], Zhipeng Shao[1], Xiaosha Cui[1], Qing Su[1] and Erqing Xie[1]*

[1]Key Laboratory for Magnetism and Magnetic Materials of the Ministry of Education, School of Physical Science and Technology, Lanzhou University, Lanzhou 730000, P. R. China

*Corresponding authors

Key Laboratory for Magnetism and Magnetic Materials of the Ministry of Education, School of Physical Science and Technology, Lanzhou University, Lanzhou 730000, P. R. China

E-mail: fujc@lzu.edu.cn (J. Fu); xieeq@lzu.edu.cn (E. Xie)

[#]These authors contributed equally to this work.

Capacitance determination

To analyze quantitatively of the type of total stored charge, Dunn's method was used in analysis. In detail, two separate mechanisms: surface-controlled process (k_1v, including fast-response capacitive effect) and diffusion-controlled process ($k_2v^{1/2}$) contribute to the current response in CV curves at fixed potential according to the following equation:

$$i(V) = k_1 v + k_2 v^{1/2} \quad (1)$$

where i is the current, v is the scan rate. The fraction of current arising from two mechanisms at fixed potential can be distinguished by determining k_1 and k_2 values quantitatively.

Energy and power density calculation

The average volumetric power density P_v and energy density (E) were calculated by using the following equations (2-3):

$$E = \frac{1}{2} CV^2 \tag{2}$$

$$P_v = E_v / I\Delta t \tag{3}$$

The specific capacity can be calculated *via* the equation (4) and (5) as follows:

GCD curves:

$$C_s = \frac{Q}{m} = I\,\Delta t / m \tag{4}$$

CV curves:

$$C_s = Q/m = S/2vm \tag{5}$$

Where C_s (F g^{-1}) is the specific capacitance; Q (C) is the average charge during the charging/discharging process; m (g) is the mass loading of the active materials; S (A V) is the integrated area of the CV curve; v (V s^{-1}) is the scan rate; I (A) is the constant discharging current; Δt (s) is the discharging time.

The specific capacitance (C, F g^{-1}) can be calculated *via* the equation (6) as follows:

$$C = C_s / \Delta V \tag{6}$$

Where ΔV (V) is the potential window.

Structural and Morphological Characterization of the Electrodes

The Fe_2O_3@CNFs electrode was obtained by successive oxygen plasma exposing and annealing at 300℃ with the synthesized FeC@CNFs electrode (in Figure S1). Since the FeC nanoparticles was wrapped with the carbon wall in the FeC@CNFs nanofibers due to the catalytic carbonization effect, the procedure of oxygen plasma treatment was adopted to break and etch away the bondage of the carbon wall, ensuring the bareness of the FeC nanoparticles. A following high-temperature annealing process converts the bare FeC to Fe_2O_3, which results to the formation of Fe_2O_3@CNFs electrode, as illustrated in Figure S2. Fe_2O_3 in the Fe_2O_3@CNFs electrode is evenly distributed on the outer surface of the carbon nanofiber and has a higher oxidation state. XPS was further used to investigate the chemical composition of the Fe_2O_3@CNFs, O-FeC@CNFs and FeC@CNFs. Core-level Fe 2p spectrum (Figure S3a) reveals two distinct peaks at the binding energies of 711.1 eV for Fe $2p_{3/2}$ and 724.7 eV for Fe $2p_{1/2.}$ The swing around the satellite peak at 719.0eV confirms the increase in the valence of the element Fe[1]. The O 1s peak can be deconvoluted into three peaks of H-O-H (533.1eV), Fe−O−H (531.3 eV) and Fe−O−Fe (529.9 eV) (Figure S3b)[2]. The specific gravity of the lattice oxygen in Fe_2O_3@CNFs is obviously increased, which is also consistent with the ratio of Fe, O and C elements in these three samples (Figure S3c). The crystal structure of Fe_2O_3@CNFs, O-FeC@CNFs and FeC@CNFs were further verified by Raman and XRD methods. Further Raman spectra of the pristine Fe_2O_3@CNFs, O-FeC@CNFs and FeC@CNFs were shown in Figure S3d. It can be found that the D-band located at 1344 cm^{-1} and the G-band at 1594 cm^{-1} are the characteristic Raman shift of carbonaceous materials. And Fe_2O_3@CNFs have completer and more obvious five Raman shifts at 220, 287, 397, 480 and 600 cm^{-1} can be ascribed to α-Fe_2O_3 than the other two samples[3]. Figure S3e displays the XRD patterns of the pristine Fe_2O_3@CNFs, O-FeC@CNFs and FeC@CNFs. Despite the typical peaks from carbonaceous materials, Fe_2O_3@CNFs removed the phase of FeC and showed show

three diffraction peaks in 33.0°, 35.6° and 49.4°, which can be indexed to the (104), (110) and (024) reflections of α-Fe_2O_3 (JCPDS No. 33-0664), compared to FeC@CNFs and O-FeC@CNFs. The Fe_2O_3@CNFs structures were further demonstrated by TEM observations. A representative TEM image (Figure S4a and b) displays that the Fe_2O_3 NPs were uniformly distributed on the carbon nanowire fiber. Magnified image coming from a single Fe_2O_3@CNFs (Figure 2c) reveals the obvious lattice fringes, and the interplanar spacings are 0.270 nm, which correspond to the (104) crystal planes of the Fe_2O_3 in the core regions, respectively. Elemental maps derived from the EDS spectra image of an individual Fe_2O_3@CNFs manifest the location of CNF and Fe_2O_3, as shown in Figure S4c-3f. The Fe and O elements are distributed evenly around the carbon nanowire fiber.

High-resolution Mn 2p spectrum (Figure S6a) shows two pairs of typical peaks, belonging to Mn^{4+} and Mn^{3+}. The peaks, located at 653.4 and 641.7 eV with a spin-energy separation of 11.7 eV, are the characteristic spin–orbit peaks of Mn $2p_{1/2}$ and Mn $2p_{3/2}$, respectively[4]. Figure S6b shows the XPS spectra of Mn 3s core level[5]. The presence of three deconvoluted peaks in the O 1s spectrum (Figure S6c), at the binding energies of 529.6, 530.9, and 532.5 eV, represents the Mn-O-Mn, Mn-O-H, and H-O-H[6]. The XPS spectrum of N 1s is displayed in Figure S6d. The broad band of N 1s has been fitted into typical peaks for PAN with binding energies of 399.8, corresponding to -C≡N, respectively[7]. Figure S6f shows the XRD patterns of the pristine CNTs/PAN and MnO_2@CNTs/PAN composite. Except for the CNTs and PAN, all other diffraction peaks can be indexed to birnessite-MnO_2 (JCPDS No. 18-0802).

Electrochemical Characterization of the Anode

the electrochemical performance of the FeC@CNFs, O-FeC@CNFs and Fe_2O_3@CNFs based electrodes was evaluated in a three-electrode configuration with 0.5 M NaCl electrolyte working in a negative potential window of -1.2-0 V (vs. SCE). Figure S9a shows the typical CV curves of

FeC@CNFs, O-FeC@CNFs and Fe_2O_3@CNFs at the scan rate of 5 mV s^{-1}, where only the Fe_2O_3@CNFs/NaCl system shows the peak of the reversible redox reaction. Figure S9b displays representative GCD curves of FeC@CNFs, O-FeC@CNFs and Fe_2O_3@CNFs collected at the current density of 2 A g^{-1}. Fe_2O_3@CNFs exhibits more substantially longer charge and discharge time than that of FeC@CNFs and O-FeC@CNFs, indicating the better charges storage capability of Fe_2O_3@CNFs. It is worth noting that the GCD curve of the Fe_2O_3@CNFs manifests more tortuous than that of FeC@CNFs and O-FeC@CNFs, which demonstrates Fe_2O_3@CNFs possesses a more superior pseudocapacitor behavior. We can also draw from the electrochemical impedance spectroscopy (EIS) (Figure S9c) that Fe_2O_3@CNFs has the equivalent series resistance and charge transfer resistance with oxygen plasma and high temperature annealing break the bondage of amorphous carbon and improve the oxidation state of Fe. The specific capacities of the FeC@CNFs, O-FeC@CNFs and Fe_2O_3@CNFs as a function of scan rate are compared in Figure S9d. As expected, the Fe_2O_3@CNFs system shows much higher specific capacities at all the scan rates from 5 mV s^{-1} to 100 mV s^{-1} when compared to the FeC@CNFs and O-FeC@CNFs. Additionally, the long-term cycling stability of the FeC@CNFs, O-FeC@CNFs and Fe_2O_3@CNFs were evaluated at a slow scan rate of 2 A g^{-1} for 5000 cycles (Figure S9e). Similarly, after 5000 cycles, FeC@CNFs has the most excellent cycle stability.

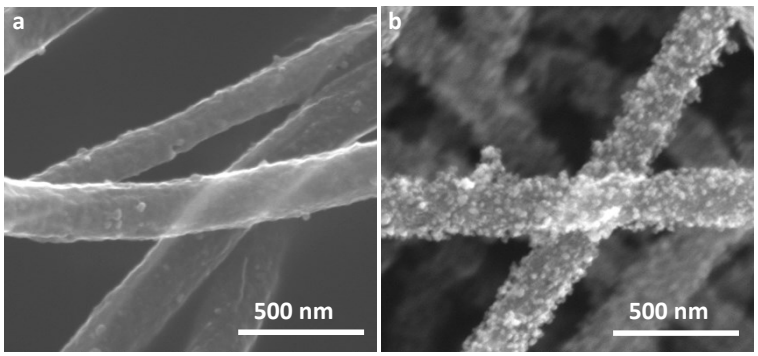

Figure S1: SEM images of the FeC@CNFs and O-FeC@CNFs.

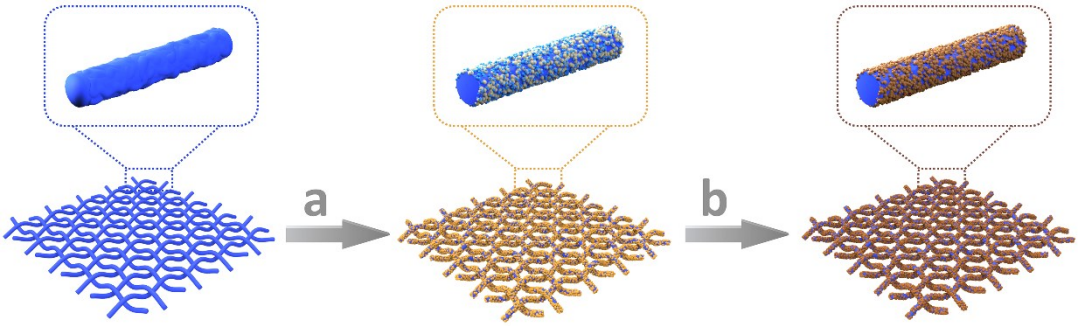

Figure S2: Schematic illustration of the preparation procedure of the Fe_2O_3@CNFs.

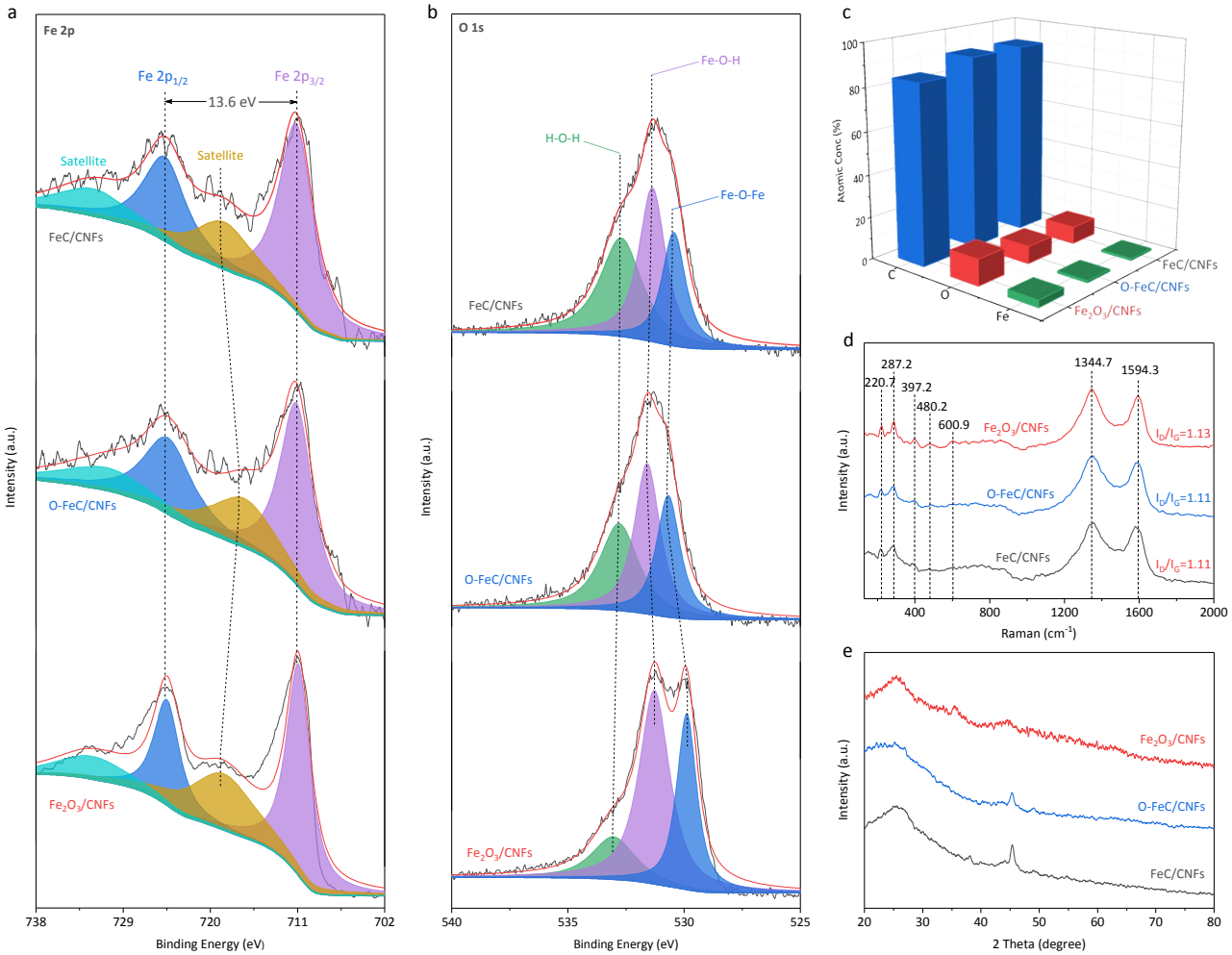

Figure S3: Structural and chemical characterizations of Fe_2O_3@CNFs, O-FeC@CNFs and FeC@CNFs. (a) Fe 2p and (b) O 1s core-level XPS spectrum; (c) element content; (d) Raman spectra and (e) XRD patterns of Fe_2O_3@CNFs, O-FeC@CNFs and FeC@CNFs.

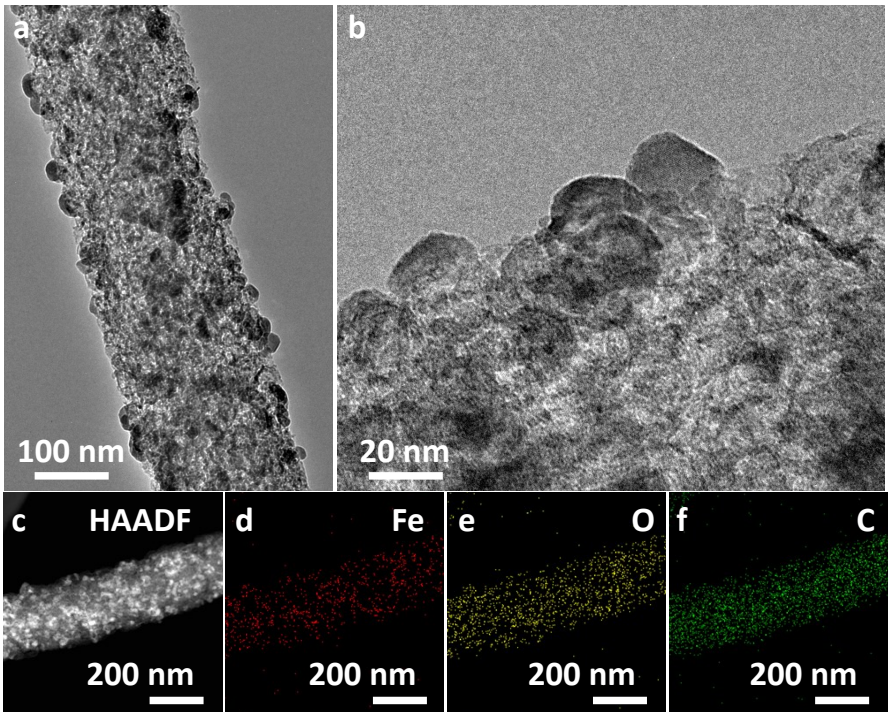

Figure S4: (a) and (b) TEM images; (c-f) elements distribution of Fe, O and C for an individual Fe_2O_3@CNFs.

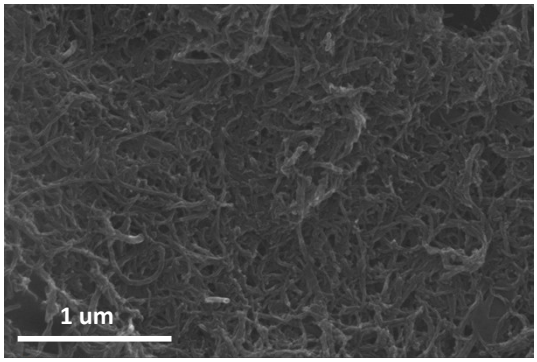

Figure S5: SEM images of the CNTs.

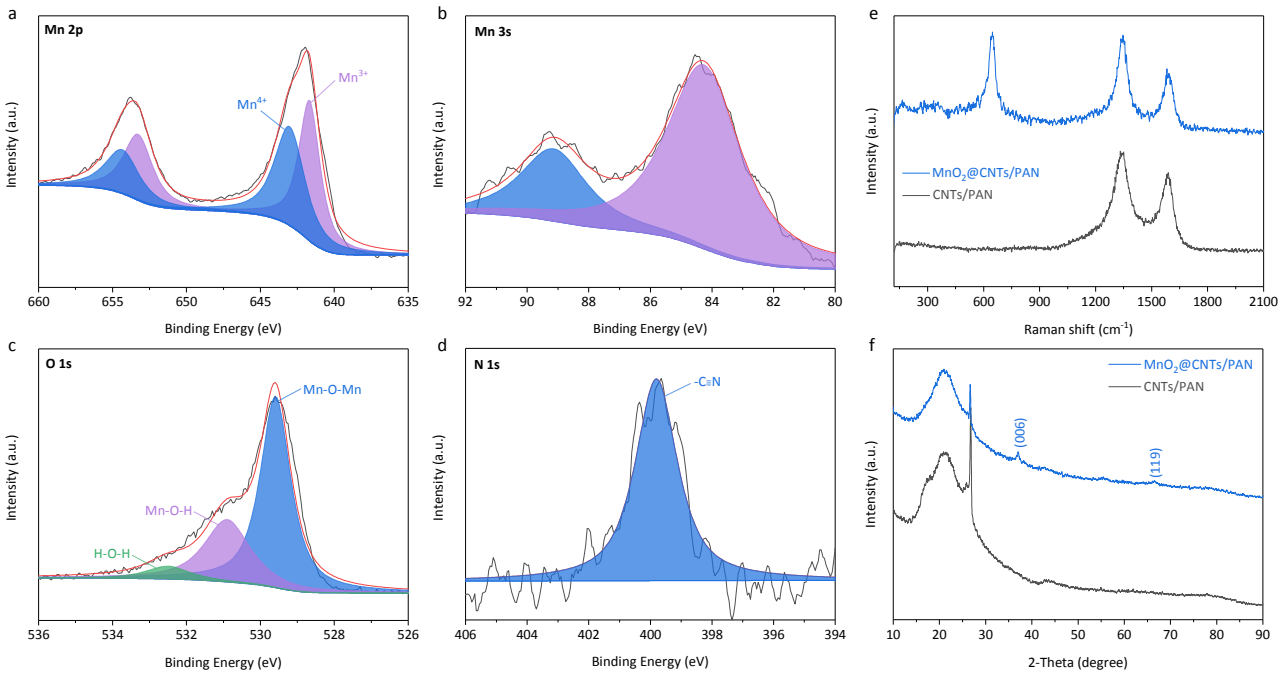

Figure S6: Structural and chemical characterizations of MnO_2@CNTs/PAN. (a) Mn 2p; (b) Mn 3s; (c) O 1s and (d) N 1s core-level XPS spectrum; (e) Raman spectra and (f) XRD patterns of MnO_2@CNTs/PAN and CNTs/PAN.

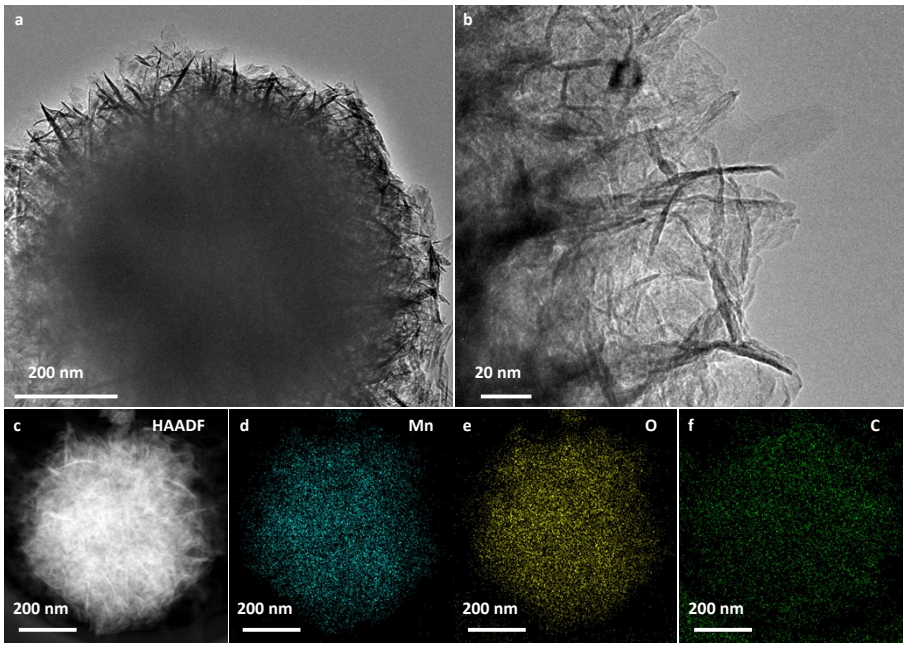

Figure S7: (a) and (b) TEM images; (c-f) elements distribution of Mn, O and C for an individual Fe_2O_3@CNFs.

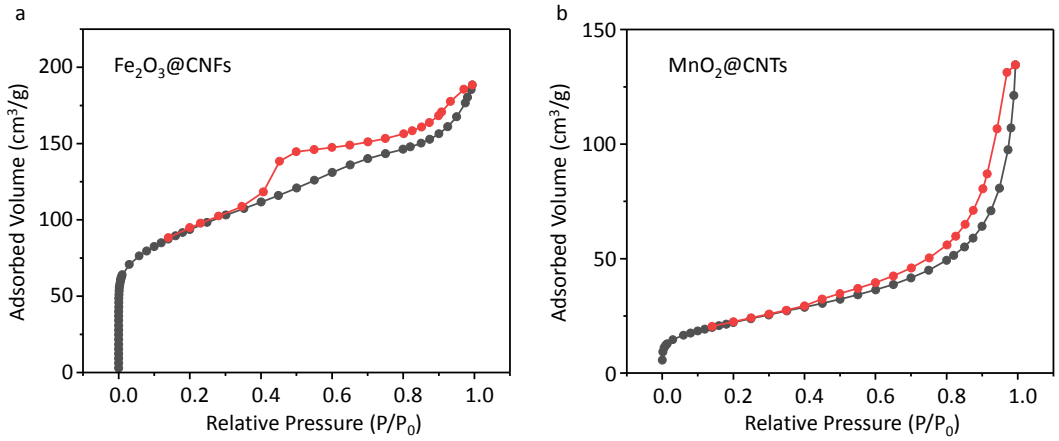

Figure S8: Nitrogen adsorption-desorption isotherms of (a) Fe_2O_3@CNFs and (B) MnO_2@CNTs.

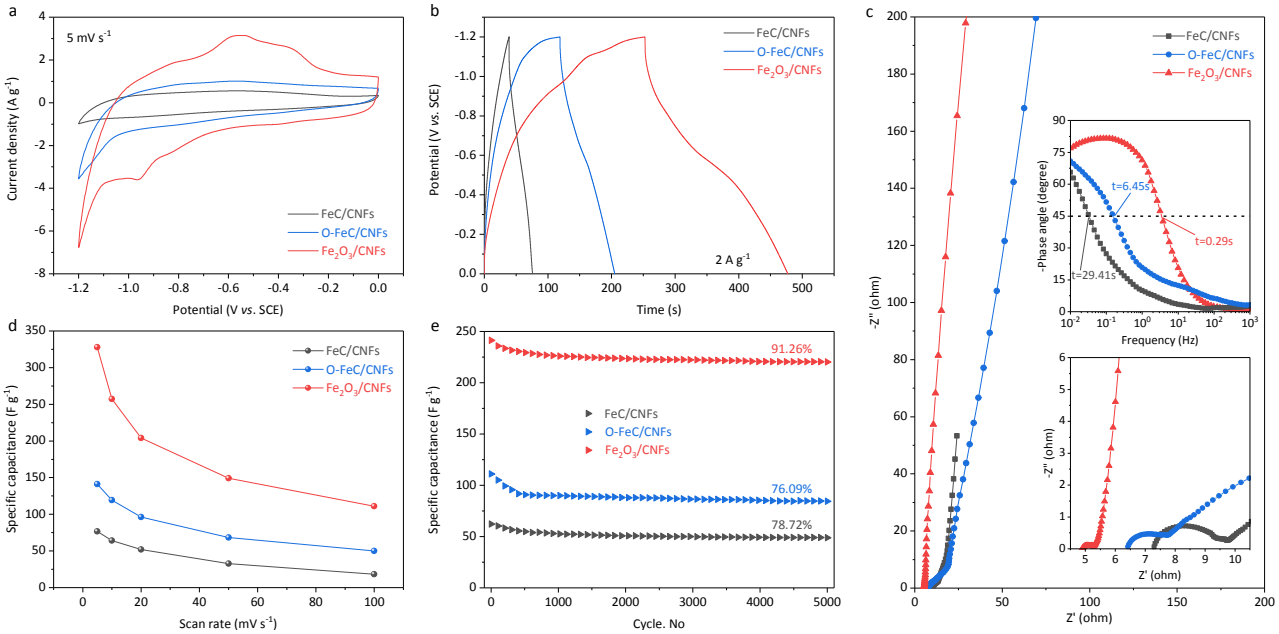

Figure S9: Comparative electrochemical performance of FeC@CNFs, O-FeC@CNFs and Fe_2O_3@CNFs based electrodes in 0.5 M NaCl electrolyte. (a) Typical CV curves collected at scan rate of 5 mV s^{-1}; (b) GCD curves recorded at current density of 2 A g^{-1}; (c) Nyquist plots and Bode plots (d) Specific capacitance as a function of scan rate derived from the CV curves; (e) Cycling performance operated at 1 A g^{-1} for 5000 cycles.

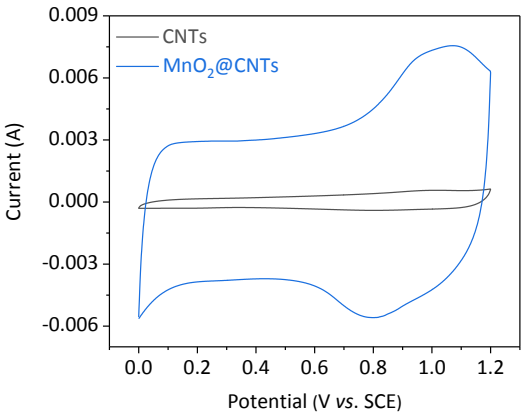

Figure S10: CV curves of the MnO_2@CNTs and CNTs electrode in 0.5 M NaCl electrolyte at scan rate of 5 mV s^{-1}.

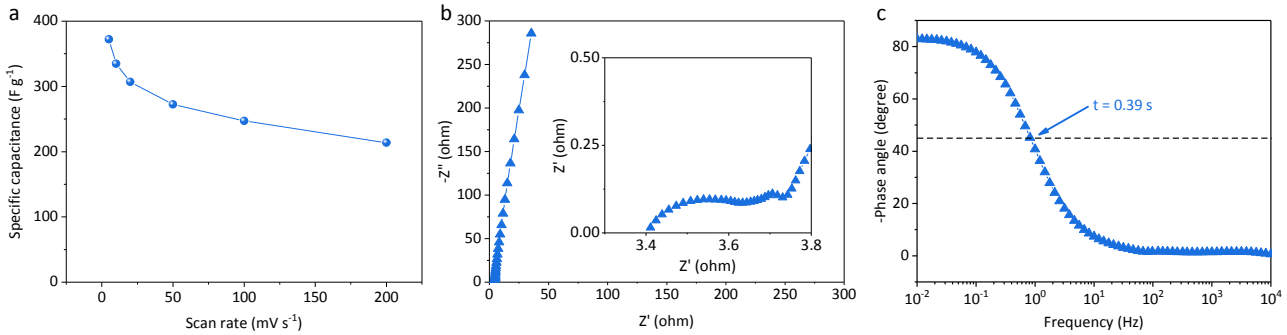

Figure S11: Electrochemical performance of the MnO_2@CNTs electrode. (a) Specific capacitance as a function of scan rate derived from the CV curves; (b) Nyquist plots; (c) Bode plots.

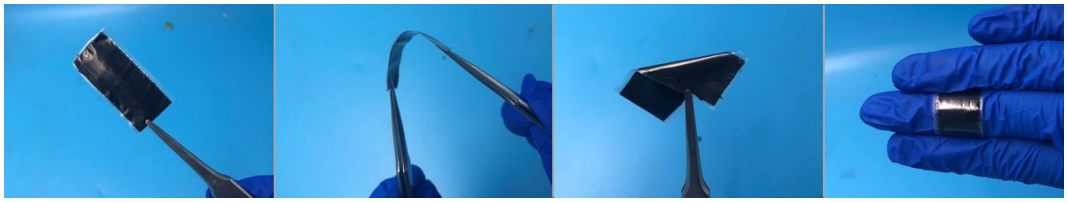

Figure S12: Optic images of the all-in-one ASC

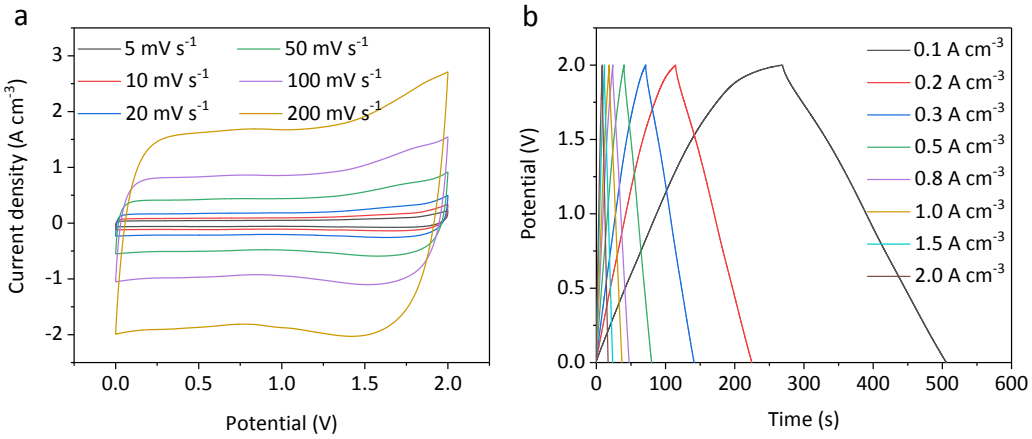

Figure S13: (a) CV curves over various scan rates, (b) GCD curves over various current densities.

Table S1. Electrochemical Performance of Reported All-in-one Supercapacity in Recent Papers

SCs devices	Capacitance ($F\ g^{-1}$)	Power density ($W\ kg^{-1}$)	Energy density ($Wh\ kg^{-1}$)	ref
Fe_2O_3@CNFs//MnO_2@CNTs	79	667	43.1	Our work
Graphene SCSPC	36.6	750	35.6	8
MWCNT/MoO_3	48.3	100	13.2	9
NS-SHC//NS-SHC	73	250	10.2	10
$PNGs_{300-800}$//$PNGs_{300-800}$	84.8	650	19.9	11
MnO_2 NWs//FeOOH NSs	70	393	24.8	12

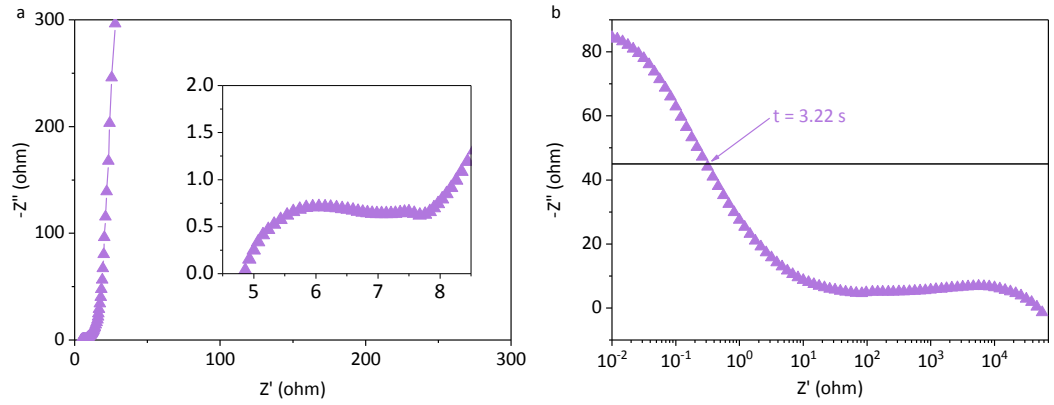

Figure S14: Electrochemical performance of the all-in-one supercapacitor. (a) GCD curves of the all-

in-one ASC device operated in different voltage windows; (b) Nyquist plots; (c) Bode plots.

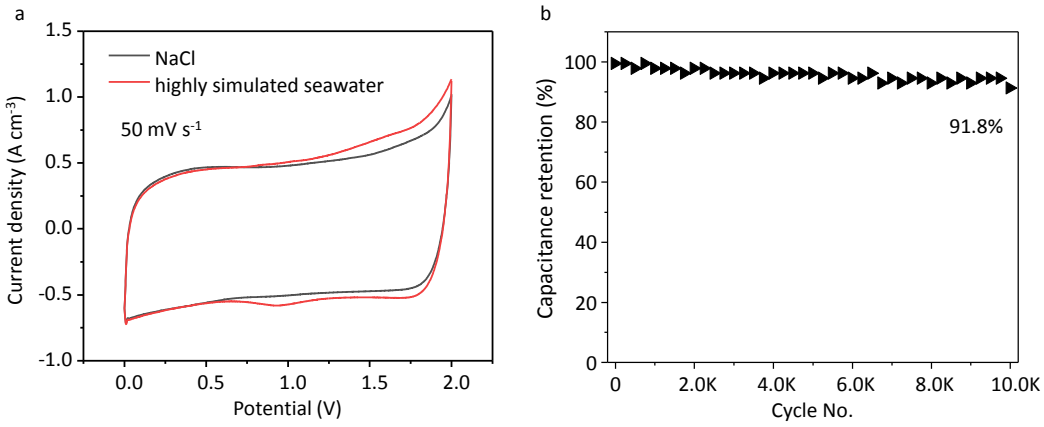

Figure S15: (a) CV curves of the "paper-like" all-in-one supercapacitor cell in NaCl-based electrolyte and highly seawater-simulated electrolyte at a scan rate of 50 mV^{-1}; (b) Cycling performance of the supercapacitor in the highly seawater-simulated electrolyte at a current density of 4 A g^{-1}.

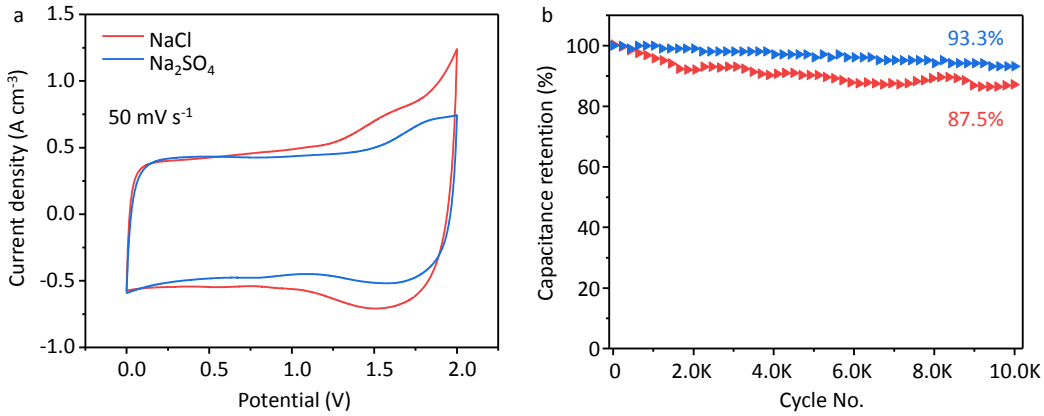

Figure S16: (a) CV curves of the paper-like all-in-one supercapacitor cell in NaCl electrolyte and Na_2SO_4 electrolyte at a scan rate of 50 mV^{-1}; (b) Cycling performance of the supercapacitor in Na_2SO_4 electrolyte at a current density of 4 A g^{-1}.

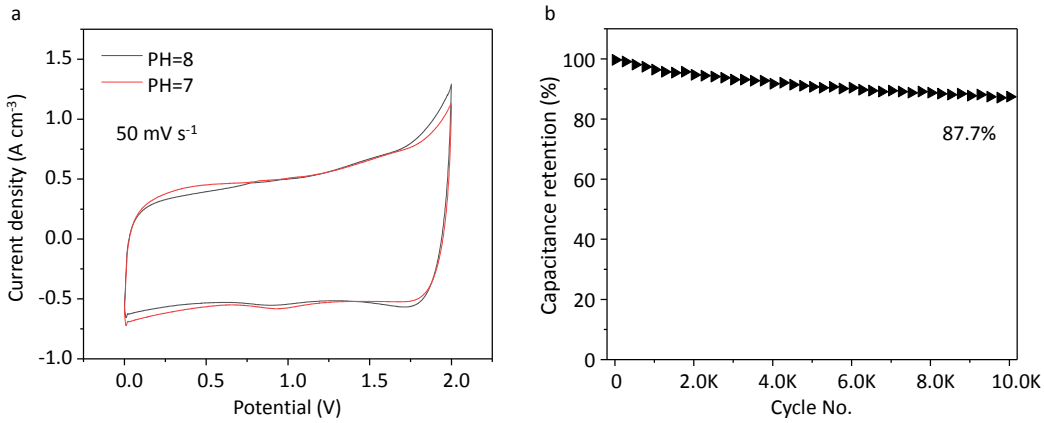

Figure S17: (a) CV curves of the paper-like all-in-one supercapacitor cell in NaCl electrolyte at pH=7 and pH=8 at a scan rate of 50 mV^{-1}; (b) Cycling performance of the supercapacitor in Na_2SO_4 electrolyte at pH=8 at a current density of 4 A g^{-1}.

REFERENCES

1. T. Yamashita and P. Hayes, Appl Surf Sci, 2008, **254**, 2441-2449.
2. J. Y. Seok, J. Lee, J. H. Park and M. Yang, Adv Energy Mater, 2019, **9**, 1803764.
3. J. Zhao, Z. Li, X. Yuan, Z. Yang, M. Zhang, A. Meng and Q. Li, Adv Energy Mater, 2018, **8**, 1702787.
4. C. Liu, X. Chi, Q. Han and Y. Liu, Adv Energy Mater, 2020, **10**, 1903589.
5. M. Mateos, N. Makivic, Y. S. Kim, B. Limoges and V. Balland, Adv Energy Mater, 2020, **10**, 2000332.
6. M. Li, Q. He, Z. Li, Q. Li, Y. Zhang, J. Meng, X. Liu, S. Li, B. Wu, L. Chen, Z. Liu, W. Luo, C. Han and L. Mai, Adv Energy Mater, 2019, **9**, 1901469.
7. L. Wang, H. Yang, X. Liu, R. Zeng, M. Li, Y. Huang and X. Hu, Angew Chem Int Ed, 2017, **56**, 1105-1110.
8. S. Sahoo, K. Krishnamoorthy, P. Pazhamalai, V. K. Mariappan, S. Manoharan and S.-J. Kim, J Mater Chem A, 2019, **7**, 21693-21703.
9. H. Park, J. W. Kim, S. Y. Hong, G. Lee, H. Lee, C. Song, K. Keum, Y. R. Jeong, S. W. Jin, D. S. Kim and J. S. Ha, ACS Nano, 2019, **13**, 10469-10480.
10. C. Liu, F. Yi, D. Shu, W. Chen, X. Zhou, Z. Zhu, R. Zeng, A. Gao, C. He and X. Li, Electrochim Acta, 2019, **319**, 410-422.
11. S. Li, N. Zhang, H. Zhou, J. Li, N. Gao, Z. Huang, L. Jiang and Y. Kuang, Appl Surf Sci, 2018, **453**, 63-72.
12. T. Gao, Z. Zhou, J. Yu, D. Cao, G. Wang, B. Ding and Y. Li, Acs Appl Mater Interfaces, 2018, **10**, 23834-23841.